JOURNAL OF THERMOPHYSICS AND HEAT TRANSFER
Vol. 8, No. 1, Jan.–March 1994

Evaporating Extended Meniscus in a V-Shaped Channel

L. W. Swanson* and G. P. Peterson†
Texas A&M University, College Station, Texas 77843

A mathematical model of the evaporating extended meniscus in a V-shaped channel was developed to investigate the effect of wedge half-angle and vapor mass transfer on meniscus morphology, fluid flow, and heat transfer. The liquid was unsaturated, flowed down the wedge due to gravity, and evaporated into atmospheric air. The average Nusselt number was found to decrease as the wedge half-angle increased, primarily because of an increase in the average wall-interface temperature difference. The mean curvature changed from zero at the interline to a constant, at a distance approximately three times the adsorbed layer thickness from the wall. The capillary pressure calculated from first principles was nearly twice as large as that determined from a semicircular approximation of the mean curvature. We believe that this was partially due to the presence of the van der Waals attraction near the wall. Downstream from the inlet, both thermocapillary convection and pressure recovery in the liquid caused the interline to move downward toward the wedge apex and then upward away from the apex until the piezometric pressure gradient was equal to zero. The locus of liquid dry out points were estimated based on axial locations where the piezometric pressure gradient was equal to zero; this represented a point of zero flow in the channel. As expected, the points where dry out occurred, moved closer to the inlet as the surface mass flux was increased.

Nomenclature

a = aspect ratio, r_0/L
Ca = capillary number
E = evaporation number
F = surface mass transfer number
G = arc-length function
$\hat{g}$ = gravity vector
H = mean curvature of the vapor-liquid interface
h = heat transfer coefficient at a given axial location
h_{ave} = average heat transfer coefficient
h_{fg} = latent heat of vaporization
h_m = mass transfer coefficient
I = identity tensor
J = mass flux at the interface
k = thermal conductivity in the liquid
M = Marangoni number
$M_{\hat{n}}$ = magnitude of the normal vector
$M_{\hat{t}}$ = magnitude of the tangent vector
m = summation index
Nu_{ave} = average Nusselt number
$\hat{n}$ = unit normal vector to the interface pointing into the vapor phase
P = pressure
Pr = Prandtl number
R = radial location of the vapor-liquid interface
R_{vap} = gas constant divided by the molecular weight of the vapor
r = radial spatial coordinate
r_0 = interline location at the wedge inlet
T = temperature
$\hat{t}$ = unit tangent vector to the interface
u = radial velocity
v = azimuthal velocity
$\hat{v}$ = velocity vector
w = axial velocity
z = axial spatial coordinate
z steps = number of steps in the axial direction
∇ = gradient operator
α = wedge half-angle
β = wedge inclination angle with respect to the gravity vector
γ = change in surface tension with respect to temperature
Δr = radial spatial increment
Δz = axial spatial increment
$\Delta\theta$ = azimuthal spatial increment
δ = adsorbed layer thickness
$\hat{\delta}_r$ = unit vector in the radial direction
$\hat{\delta}_z$ = unit vector in the axial direction
$\hat{\delta}_\theta$ = unit vector in the azimuthal direction
ε = azimuthal coordinate with an origin at the wall, $\alpha - \theta$
ε_0 = angle associated with the adsorbed layer thickness
θ = azimuthal spatial coordinate
κ = thermal diffusivity in the liquid
μ = dynamic viscosity in the liquid
Π = disjoining pressure
ρ = density in the liquid
σ = surface tension
τ = rate of deformation tensor
ϕ = local contact angle with the wall

Subscripts

a = atmospheric conditions
a,sat = saturated conditions at atmospheric pressure
i = vapor (same species as the liquid)
r = derivative with respect to the radial direction
z = derivative with respect to the axial direction
w = wall
0 = at the interline
θ = derivative with respect to the azimuthal direction

Superscripts

g = gas phase
I = interface

Received Oct. 13, 1992; revision received March 10, 1993; accepted for publication March 11, 1993.

*Currently at HTRI, 1500 Research Parkway. Member AIAA.
†Tenneco Professor of Engineering, Mechanical Engineering Department. Associate Fellow AIAA.

Introduction

EVAPORATING a liquid flowing down a plate composed of small channels has applications in many areas of ther-

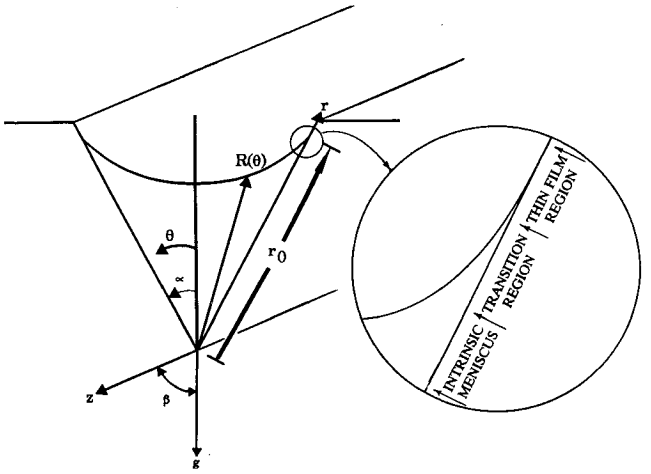

Fig. 1 Wedge coordinate system and length scales.

mal technology such as plate evaporators, desalinization heat exchangers, and heat pipes. In some cases the surface of a gravity-driven plate evaporator is machined or etched into an array of parallel V-shaped channels between 10–300 μm on a side. The channels prevent the formation of rivulets typical of evaporating thin films flowing down an inclined flat plate due to gravity. Rivulets are undesirable because they decrease the contact area between the liquid and the wall, and thus prevent the efficient use of available hot wall heat transfer area for evaporation. The grooved configuration also provides a larger evaporation surface area than a thin film of liquid, due to the curvature of the meniscus, while sustaining the large wall-to-meniscus temperature gradients common to thin liquid films. For saturated wetting liquids, the grooved configuration also takes advantage of the large heat transfer rates characterizing evaporation in the submicron layer near the interline (triple-contact line).

Figure 1 depicts an evaporating meniscus in an isolated V-shaped channel with a constant surface temperature. The liquid is unsaturated and evaporating into air. α and β are measured with respect to the gravity vector. Liquid enters the top of the channel at a temperature lower than the liquid saturation temperature. For inclination angles less than 90 deg, the liquid flows downward due to gravity and a meniscus develops whether the fluid is heated by the wall or not. The morphology of the isothermal meniscus, which in this case serves as an initial condition at the channel entrance, is dependent on the surface forces near the interline and surface tension forces characterizing the intrinsic meniscus. Wall cooling occurs downstream where liquid evaporates at the interface forcing a liquid temperature gradient between the wall and the meniscus. The evaporation rate at the interface is dependent on both the flow conditions in the gas and the magnitude of the vapor pressure driving force (or concentration driving force). Evaporation, or wall cooling, subsides when the partial pressure of the vapor at the interface is equal to the partial pressure of the vapor in the bulk gas; this negates the driving force for vapor mass transfer.

Literature Survey

Investigations of the surface wetting and fluid flow in small capillary grooves have been conducted by several investigators. Early contributions were made by Bressler and Wyatt[1] who investigated the effects of capillary grooves on surface wetting in an effort to obtain expressions for predicting the variations in heat transfer conditions and optimizing groove designs. Numerical evaluation of the heat transfer rates were computed for grooves with triangular, semicircular and square cross sections. As a follow-up to this work, Ayyaswamy et al.[2] solved the two-dimensional equations of motion for steady laminar flow in triangular shaped grooves using Galerkin boundary methods. Given the liquid channel half-angle and the contact angle of the shear-free meniscus, relationships for determining the friction factor coefficient and Reynolds number (based upon the hydraulic diameter) were identified. The analytical results were compared with experimental data obtained for channel half-angles ranging from 5 to 60 deg, and contact angles from 0.1 to the full groove condition. The analytical results and experimental data exhibited a strong correlation over the entire range of both channel and contact angles.

The potential for using small channel devices in electronic cooling stimulated several studies.[3,4] In the first of these, the steady-state behavior of a trapezoidal microheat pipe 57-mm long with a 1-mm^2 cross section was investigated. The corners of the trapezoidal cross section served as grooved channels for the transport of liquid from the condenser to the evaporator. The experimental results were compared with an analytical model and were found to accurately predict the maximum heat transport capacity of the pipe. The interest in developing smaller microheat pipes prompted the study of Peterson et al.[4] An experimental investigation was undertaken to verify the microheat pipe concept for a trapezoidal pipe with a cross-sectional dimension of 30 μm. The substrate material was a silicon wafer and the working fluid was methanol. The results showed that the effective thermal conductivity increased by 25% after the empty pipe was charged with the methanol working fluid. Although these two studies indirectly addressed flow in microchannels, questions were raised concerning the role that the disjoining pressure plays in the transport of liquid from the condenser to the evaporator, especially when the cross-sectional dimension is less than 100 μm.

In addition to the aforementioned investigations involving the shape and distribution of liquid menisci in small capillary grooves, several investigations have been conducted which are directly related to thin film evaporation from grooved surfaces. Edwards et al.[5] demonstrated that a power-law solution exists for the capillary flow supplying liquid to the tip of an evaporator fin. This solution indicated that the heat transfer was limited by the fluid properties alone, and gave some indication of the magnitude of the heat transfer that could be accurately predicted for various combinations of materials. Two more recent investigations have focused specifically on the evaporation from small triangular microgrooves under supersaturated liquid flow conditions.[6,7] These two investigations developed analytical models for evaluating and predicting the heat transfer characteristics during film evaporation from microgroove surfaces. In both cases the flow was assumed to be driven by capillary pressure due to the recession of a meniscus into the groove similar to that which would occur during evaporation. In both cases the application of interest was heat pipe wicking structures. This work was later extended, and a correlation between the Nusselt number and a nondimensional parameter relating the surface and fluid properties, groove geometry, and disjoining pressure.[6,7] The results when compared with an experimental study of vaporization from a liquid coolant on a flat microgroove surface indicated that the disjoining pressure plays a significant role in the evaporation process and increases in significance as the diameter of the channels decreases.

While all of the aforementioned investigations have provided significant insight into the behavior of liquid flow and evaporation in small channels (most have focused on the intrinsic meniscus which is that portion of the meniscus characterized only by surface tension forces), only one study[7] addresses the submicron region near the interline where the solid substrate plays an important role in thin film behavior. The majority of these studies address liquids which are either saturated or mildly supersaturated. In this study we have developed a mathematical model of the extended meniscus in a V-shaped channel for an unsaturated wetting liquid evaporating into air. The formulation of the model accounts for phenomena in both the intrinsic meniscus and the interline

region. The following sections provide a detailed description of the mathematical model including the important assumptions, governing equations, boundary and interfacial conditions, scaling, and numerical procedure.

One-Sided Formulation

The mathematical model of the evaporating meniscus developed in this study applies the so-called one-sided model used by Burelbach et al.[8] This approach assumes that the density, viscosity, and thermal conductivity are much greater in the liquid phase than in the vapor phase. Furthermore, the velocity and temperature gradients in the vapor phase are assumed to be much less than those in the liquid phase. These assumptions can be applied to interfaces which are evaporating relatively slowly into an unconfined gas phase (i.e., open air).

A derivation of the governing transport equations for interfacial problems can be found in a number of reference books.[9,10] We have chosen to use the compact vector form of the governing equations given by Burelbach et al.[8]; hence, the remaining discussion of the one-sided formulation follows this reference closely.

Figure 1 shows the cylindrical coordinate system used to describe the V-shaped channel. The radial center is located at the apex of the wedge, while the origin of the azimuthal angle (θ) is placed at the wedge symmetry plane. The axial direction is perpendicular to the r-θ plane as shown in Fig. 1. $R(\theta)$ is the radial location of the meniscus and is a function of θ. r_0 is the radial location of the interline at the inlet to the channel. Note that downstream of the wedge inlet, the location of the interline can change. An adsorbed layer exists in the region above the interline whose thickness is dependent on the disjoining pressure. The magnitude of the disjoining pressure is a function of the intermolecular forces between the wall, adsorbed layer, and gas phase. Unless stated otherwise, the equations developed herein are based on the one-sided assumption and apply to the bulk liquid phase. Interfacial and gas phase variables are given by superscripts (I) and (g), respectively. In cylindrical coordinates, the outward normal vector (pointing into the gas phase) and tangent unit vectors at the interface are

$$\hat{n} = \frac{1}{M_{\hat{n}}}[\hat{\delta}_r(R) + \hat{\delta}_\theta(-R_\theta) + \hat{\delta}_z(-RR_z)] \tag{1}$$

$$\hat{t} = \frac{1}{M_{\hat{t}}}[\hat{\delta}_r(2R_\theta R_z) + \hat{\delta}_\theta(RR_z) + \hat{\delta}_z(R_\theta)] \tag{2}$$

with magnitudes of

$$M_{\hat{n}} = (R^2 + R_\theta^2 + R^2R_z^2)^{1/2}$$

$$M_{\hat{t}} = (4R_\theta^2R_z^2 + R^2R_z^2 + R_\theta^2)^{1/2}$$

For steady incompressible flow conditions the Navier-Stokes equations reduce to

$$\rho\hat{v}\cdot\nabla\hat{v} = -\nabla P + \mu\nabla^2\hat{v} + \rho\hat{g} \tag{3}$$

The continuity and energy equations for the liquid phase are

$$\nabla\cdot\hat{v} = 0 \tag{4}$$

$$\hat{v}\cdot\nabla T = \kappa\nabla^2 T \tag{5}$$

The scalar azimuthal boundary conditions at the symmetry plane are

$$\theta = 0, \qquad u_\theta = v = w_\theta = T_\theta = R_\theta = 0$$

No-slip conditions, a constant wall temperature, and appropriate interfacial conditions are imposed at the wall:

$$\theta = \alpha, \qquad \hat{v} = 0, \qquad T = T_w$$

$$R_\theta = R\cot(\alpha); \qquad P^{(g)} - P = \Pi_0$$

The total gas pressure $P^{(g)}$ is assumed to be constant. The third condition, which applies to wetting liquids, requires that the slope of the interface at the interline be equal to the slope of the wedge wall. The fourth condition given above (capillary pressure condition) evolves from interface thermodynamics and can be used to evaluate the adsorbed layer thickness.[11-23] Further discussion of the capillary pressure azimuthal boundary condition, based on scaling arguments, can be found in Ref. 20. A jump mass balance at the interface requires that the liquid and vapor mass flux normal to the interface are equal:

$$J = \rho\hat{v}\cdot\hat{n} = \rho_i^{(g)}\hat{v}_i^{(g)}\cdot\hat{n} \tag{6}$$

Since evaporation occurs in air and the liquid is unsaturated, $\rho_i^{(g)}$ is the vapor density which is only a fraction of the total gas density. The jump energy balance at the interface is

$$Jh_{fg} + k\nabla T\cdot\hat{n} = 0 \tag{7}$$

The normal stress jump condition is

$$[P^{(g)} - P]I\cdot\hat{n}\cdot\hat{n} + 2\mu\tau\cdot\hat{n}\cdot\hat{n} = 2H\sigma(T) + \Pi \tag{8}$$

where H is given by

$$2H = -\nabla\cdot\hat{n} \tag{9}$$

The shear stress jump condition is

$$[P^{(g)} - P]I\cdot\hat{n}\cdot\hat{t} + 2\mu\tau\cdot\hat{n}\cdot\hat{t} = \nabla\sigma\cdot\hat{t} \tag{10}$$

The term on the right side accounts for thermocapillary convection (Marangoni effects). The gradient of the surface tension can be evaluated using

$$\sigma = \sigma^{(g)} - \gamma[T^{(i)} - T^{(g)}] \tag{11}$$

and the chain rule.[11,20] $\sigma^{(g)}$ is the surface tension at the bulk gas temperature $T^{(g)}$. No-slip conditions are assumed to hold at the interface requiring

$$\hat{v}\cdot\hat{t} = \hat{v}^{(g)}\cdot\hat{t}$$

Assuming the vapor mass flux is relatively small, equilibrium conditions can be imposed at the interface making the partial pressure of the evaporating liquid equal to the saturation pressure at the interface temperature. This relationship is given by the Clausius-Clapeyron equation

$$P_i^{(g)} = P_a \exp\left\{-\frac{h_{fg}}{R_{\text{vap}}}\left[\frac{1}{T^{(I)}} - \frac{1}{T_{a,\text{sat}}}\right]\right\} \tag{12}$$

The reference conditions in Eq. (12) are P_a and $T_{a,\text{sat}}$. In this particular study we are not interested in the specific vapor mass flow mechanism, and therefore, have used a simplified vapor mass flux condition assuming very low vapor concentration in the bulk gas phase:

$$J = \frac{h_m}{\rho^{(g)}R_{\text{vap}}T^{(g)}}P_i^{(g)} \tag{13}$$

With the mass transfer coefficient as a parameter, this expression can be used to vary the magnitude of the vapor mass flux.

Scaling

Lubrication scales are used to nondimensionalize and further reduce the number of terms in the governing equations. The scaled variables (barred variables) are

$$r = R\bar{r}, \quad \theta = \alpha\bar{\theta}, \quad z = L\bar{z}, \quad a = \frac{r_0}{L}$$

$$u = \frac{a\mu}{\rho L}\bar{u}, \quad v = \frac{a\mu}{\rho L}\bar{v}, \quad w = \frac{\mu}{\rho L}\bar{w}, \quad P = \frac{\mu^2}{\rho r_0^2}\bar{P}$$

$$T = T^{(g)} + (T_w - T^{(g)})\bar{T}, \quad J = \frac{k(T_w - T^{(g)})}{r_0 h_{fg}}\bar{J}$$

$$g_r = \frac{\mu^2}{\rho^2 r_0^2 L}\bar{g}_r$$

$$g_\theta = \frac{\mu^2}{\rho^2 r_0^2 L}\bar{g}_\theta, \quad g_z = \frac{\mu^2}{\rho^2 r_0^2 L}\bar{g}_z, \quad R = r_0\bar{R}$$

$$\Pi = \frac{\mu^2}{\rho r_0^2}\bar{\Pi}, \quad \sigma = \sigma_0(T_0)\bar{\sigma}$$

Substituting these variables into the governing equations, combining equations, and retaining terms to zeroth order in the aspect ratio yields the following system of equations:

$$\frac{1}{\bar{r}}(\bar{r}\bar{u})_{\bar{r}} + \frac{1}{\alpha^2\bar{r}}\bar{v}_{\bar{\theta}} + \bar{R}\bar{w}_{\bar{z}} = 0 \tag{14}$$

$$\bar{P}_{\bar{r}} = 0 \tag{15}$$

$$\bar{P}_{\bar{\theta}} = 0 \tag{16}$$

$$\frac{1}{\bar{r}}(\bar{r}\bar{w})_{\bar{r}} + \frac{1}{\alpha^2\bar{r}^2}\bar{w}_{\bar{\theta}\bar{\theta}} = \bar{R}^2(\bar{P}_{\bar{z}} - \bar{g}_{\bar{z}}) \tag{17}$$

$$\frac{1}{\bar{r}}(\bar{r}\bar{T})_{\bar{r}} + \frac{1}{\alpha^2\bar{r}^2}\bar{T}_{\bar{\theta}\bar{\theta}} = 0 \tag{18}$$

$$\bar{w}_{\bar{\theta}} = \bar{T}_{\bar{\theta}} = \bar{R}_{\bar{\theta}} = 0, \quad @\ \bar{\theta} = 0 \tag{19}$$

$$\bar{w} = 0, \quad \bar{T} = 1, \quad \bar{R}_{\bar{\theta}} = \alpha\bar{R}\cot\alpha$$
$$\bar{P}^{(g)} - \bar{P} = \bar{\Pi}, \quad @\ \bar{\theta} = 1 \tag{20}$$

$$\frac{E}{Pr}\left(\bar{R}^2 + \frac{1}{\alpha^2}\bar{R}_{\bar{\theta}}^2\right)^{1/2}\bar{J} = \bar{R}\bar{u} - \frac{1}{\alpha}\bar{R}_{\bar{\theta}}\bar{v} - \bar{R}\bar{R}_{\bar{z}}\bar{w}, \quad @\ \bar{r} = 1 \tag{21}$$

$$\left(\bar{R}^2 + \frac{1}{\alpha^2}\bar{R}_{\bar{\theta}}^2\right)^{1/2}\bar{J} = \frac{1}{\alpha^2}\bar{R}\bar{R}_{\bar{\theta}}\bar{T}_{\bar{\theta}} - \bar{T}_{\bar{r}}, \quad @\ \bar{r} = 1 \tag{22}$$

$$\bar{P}^{(g)} - \bar{P} = \frac{1}{Ca}\frac{\bar{\sigma}(\bar{T})\left(\frac{1}{\alpha^2}\bar{R}\bar{R}_{\bar{\theta}\bar{\theta}} - \bar{R}^2 - \frac{2}{\alpha^2}\bar{R}_{\bar{\theta}}^2\right)}{\left(\bar{R}^2 + \frac{1}{\alpha^2}\bar{R}_{\bar{\theta}}^2\right)^{3/2}} + \bar{\Pi}$$
$$@\ \bar{r} = 1 \tag{23}$$

$$\frac{1}{\alpha^2}\frac{\bar{R}_{\bar{\theta}}^2\bar{w}_{\bar{\theta}}}{\bar{R}} - \bar{R}_{\bar{\theta}}\bar{w}_{\bar{r}} = \frac{M}{Pr}\left(\bar{R}^2 + \frac{1}{\alpha^2}\bar{R}_{\bar{\theta}}^2\right)^{1/2}$$
$$\times\left(2\frac{\bar{R}_{\bar{\theta}}\bar{R}_{\bar{z}}}{\bar{R}}\bar{T}_{\bar{r}} + \bar{R}_{\bar{z}}\bar{T}_{\bar{\theta}} + \bar{R}_{\bar{\theta}}\bar{T}_{\bar{z}}\right), \quad @\ \bar{r} = 1 \tag{24}$$

$$E\bar{J} = F\exp\left\{-\frac{h_{fg}}{R}\left[\frac{1}{T_w + T_0(1 - \bar{T})} - \frac{1}{T_{a,\mathrm{sat}}}\right]\right\}, \quad @\ \bar{r} = 1 \tag{25}$$

The dimensionless groupings in the above Eqs. (14–25) are as follows:

Evaporation number

$$E \equiv \frac{C_p[T_w - T^{(g)}]}{a^2 h_{fg}}$$

Prandtl number

$$Pr \equiv \frac{\nu}{\kappa}$$

Capillary number

$$Ca \equiv \frac{\rho\nu^2}{r_0\sigma}$$

Marangoni number

$$M \equiv \frac{r_0\gamma[T_w - T^{(g)}]}{\mu\kappa}$$

Surface mass transfer number

$$F \equiv \frac{r_0 C_p h_m P_a}{a^2 k\rho^{(g)} R_{\mathrm{vap}} T^{(g)}}$$

In this study, a copper/methanol/air system was investigated with material properties evaluated at room temperature. Numerical values for the various adjustable parameters in the dimensionless groupings are $r_0 = 100\ \mu$m, $L = 1$ cm, $T_w = 323$ K, $T^{(g)} = 293$ K, $h_m = 0.1$–4.5 kg/m^{2}s, $\alpha = 10$–30 deg, $\beta = 80$ deg. Material properties were evaluated at the average temperature between the wall and the bulk gas. Based on the above parameters, numerical values for the dimensionless groupings are $a = 10^{-2}$, $E = 642$, $Pr = 5.65$, $Ca = 1.23 \times 10^{-4}$, $M = 5.28 \times 10^3$, and $F = 0.00339$–0.152.

Momentum Eqs. (15) and (16) show that the hydrostatic pressure acting in both the radial and azimuthal directions does not play a significant role in flow behavior. Secondly, the lubrication approximation points out that flow in the axial direction predominates in the intrinsic meniscus. Clearly, both gravity and the dynamic pressure gradient in the axial direction contribute to the net driving force for fluid flow. When the total gas pressure is held constant, the liquid pressure will change axially due to both viscous losses and meniscus attenuation caused by evaporation. Obviously, for flow to occur the combined effects of gravity ($g_z = g\cos\beta$), viscous losses, and evaporation must produce a negative piezometric pressure gradient [right side of Eq. (17)]. Thus, under steady flow conditions, the axial location where the piezometric pressure gradient goes to zero can be used to estimate the liquid dry out location.

As expected, scaling of the energy equation in the liquid shows that conduction is the predominate heat transfer mechanism. The total heat transfer rate is dependent on the wall temperature, the magnitude of liquid conduction, the interfacial mass flux, and the interfacial surface area.

Numerical Solution

The numerical procedure used to solve Eqs. (14–25) involved several steps. Initially, the interface morphology was determined using the normal stress interfacial condition, Eq. (23). This was done by reformulating Eq. (23) as a nonlinear

second-order initial value problem. A change of variables and reduction of order produced two coupled nonlinear ordinary differential equations. After linearizing the first-order terms, the equation set was cast in the following form:

$$\bar{R}_{\bar{\phi}} = \bar{D} \tag{26}$$

$$\bar{D}_{\bar{\phi}} = A_1^*(\bar{D} - \bar{D}^*) + A_2^* \tag{27}$$

where

$$\bar{\phi} = 1 - \bar{\theta}$$

$$A_1^* = \left[\frac{4\bar{D}}{\bar{R}} + \frac{3Ca\bar{D}(\bar{R}^2 + 1/a^2\bar{D}^2)^{1/2}(\Delta\bar{P} - \bar{\Pi})}{R}\right]^*$$

$$A_2^* = \left[\frac{2\bar{D}}{\bar{R}} + a^2\bar{R}^2 + \frac{a^2Ca(\bar{R}^2 + 1/a^2\bar{D}^2)^{3/2}}{\bar{R}}(\Delta\bar{P} - \bar{\Pi})\right]^*$$

The asterisk above refers to a constant evaluated at the previous iteration. These two equations were solved implicitly by shooting toward the boundary condition at the symmetry plane where $\bar{R}_{\bar{\theta}} = 0$. Because the slope at the interline for wetting liquids is related to the interface via $\bar{R}_{\bar{\theta}} = \alpha\bar{R}_0 \cot \alpha$, the interline location R_0 could be adjusted until the symmetry plane condition was satisfied. For a given capillary pressure difference, the adsorbed layer thickness above the interline was determined from Eq. (20). This procedure was automated using the secant method[23] with 10,001 steps to ensure sufficient spatial resolution near the interline. This method produced both the interline location and adsorbed layer thickness at each axial location. The liquid pressure, or capillary pressure difference, used for this calculation was determined from a bulk pressure correction expression discussed later. A similar procedure was used to determine the capillary pressure at the wedge inlet where the interline location was set equal to one. Note that only one unique capillary pressure and adsorbed layer thickness satisfied the boundary conditions at each axial location.

The diffusion terms in the axial momentum equation (Poisson equation) and energy equation (Laplace equation) were discretized using centered finite differencing, while upwind finite differencing was applied to the axial pressure gradient. A line-by-line method using a tridiagonal matrix algorithm (TDMA) was employed to calculate numerical values of the axial velocity and temperature. Centered finite differences were also applied to the boundary and interfacial conditions. This type of procedure can be found in most standard textbooks on numerical methods (i.e., Refs. 21 and 23).

The pressure at any cross section was evaluated using a pressure correction similar to that found in the SIMPLE algorithm of Patankar.[20] The pressure correction was based on the integral form of the continuity equation derived by integrating Eq. (14) over the entire cross-sectional domain. Application of the Leibnitz rule in combination with the kinematic condition given by Eq. (21) produced

$$\frac{d}{d\bar{z}}\int_0^1\int_0^1 \bar{R}^2\bar{w}\bar{r}\,d\bar{r}\,d\bar{\theta} = -\frac{E}{Pr}\int_0^1\left(\bar{R}^2 + \frac{1}{\alpha^2}\bar{R}_{\bar{\theta}}^2\right)^{1/2}\bar{J}\,d\bar{\theta} \tag{28}$$

The integrals in this expression were evaluated using Simpson's integration, while the differential term was discretized using upwind finite differencing. The pressure correction was found to be related to the velocity by

$$\bar{w}_{i,j}^{n+1} = \bar{w}_{i,j}^{(n+1)} + \frac{[\bar{R}_j^{(n+1)}]^2}{\Delta\bar{z}b_i}\Delta\bar{P}^{n+1} \tag{29}$$

where

$$b_i = -\frac{2\bar{r}_i\Delta\bar{\theta}}{\Delta\bar{r}} - \frac{2\Delta\bar{r}}{\alpha^2\bar{r}_i\Delta\bar{\theta}}$$

Indices written as subscripts define the cross-sectional location, whereas indices written as superscripts specify the axial location. Indices with parentheses refer to values at the previous iteration. Combining the discretized form of Eq. (28) with Eq. (29) yielded the pressure upgrade ($\Delta\bar{P}^{n+1}$) as a function of the integrated velocity distribution.

The discretized equation set was solved on an IBM RS-6000 model 320H minicomputer. Iteration continued at each cross-sectional location until all dependent variables converged to a relative error less than 10^{-5}. The discretized form of the integral continuity equation was satisfied to a relative error of less than 10^{-3}. An 80 × 80 cross-sectional grid with 0.02 increments in the axial direction produced solutions accurate to within 1%. Optimizing a relaxation factor multiplying the pressure upgrade term significantly reduced the overall run time. Run times varied between 1–4 h, depending on the parameter values.

Results and Discussion

In this study, we are interested in examining the effect wedge half-angle and vapor mass flux have on heat transfer (Nusselt number), interface morphology, axial liquid pressure gradient, and liquid dry out location. As mentioned earlier, a copper/methanol/air system was considered with material properties evaluated at room temperature.

Numerically generated heat transfer data were compiled in terms of an average Nusselt number defined as

$$Nu_{ave} = (h_{ave}r_0/k) \tag{30}$$

The axially averaged heat transfer coefficient h_{ave} found in this expression is

$$h_{ave} = \left[\sum_{m=1}^{z\,steps} h(\bar{z}_m)/z\text{ steps}\right]$$

where

$$h(\bar{z}) = \left\{\frac{k}{r_0}\int_0^1 \bar{J}(\bar{\theta}, \bar{z})G(\bar{\theta})\,d\bar{\theta}\Big/\int_0^1 [1 - \bar{T}^{(I)}]G(\bar{\theta})\,d\bar{\theta}\right\}$$

h($\bar{z}$) is the heat transfer coefficient at a given axial location. The numerator in this expression is the average surface heat flux, whereas the denominator is the average temperature difference between the wall and the interface. The function $G(\bar{\theta})\,d\bar{\theta}$ is the differential meniscus cross-sectional arc length given by

$$G(\bar{\theta})\,d\bar{\theta} = [\bar{R}^2(\bar{\theta}) + (1/\alpha^2)\bar{R}_{\bar{\theta}}^2(\bar{\theta})]^{1/2}\,d\bar{\theta}$$

Other forms of the Nusselt number based on various types of averaging and the temperature difference between the wall and the cross-sectional bulk liquid temperature were also calculated. The form given above was most convenient from a computational point of view, requiring less grid points for computational accuracy. Also, the trends exhibited by the various types of Nusselt numbers were similar in nature.

Figure 2 shows the Nusselt number as a function of the wedge half-angle. For a given wedge half-angle, the Nusselt number was found to be nearly independent of F. Therefore, an increase in the average surface heat flux is compensated by an equivalent increase in the average temperature difference between the wall and the interface. All of the numerical data fell within 2% of the curve given in Fig. 2. Furthermore, the local Nusselt number changed very little axially, because

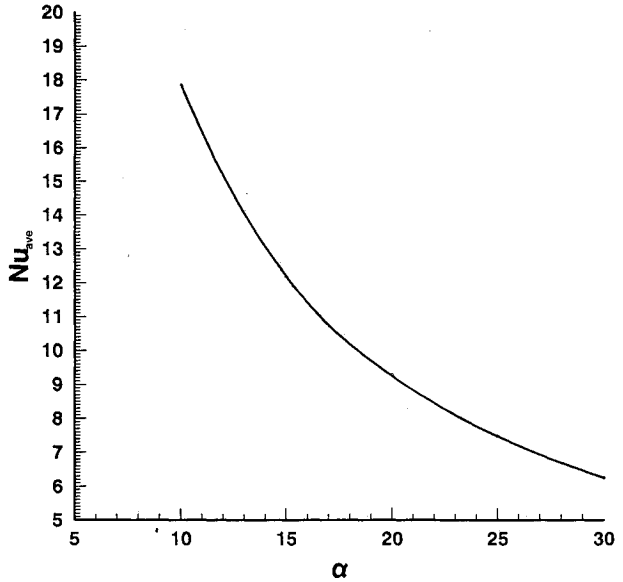

Fig. 2 Average Nusselt number as a function of wedge half-angle.

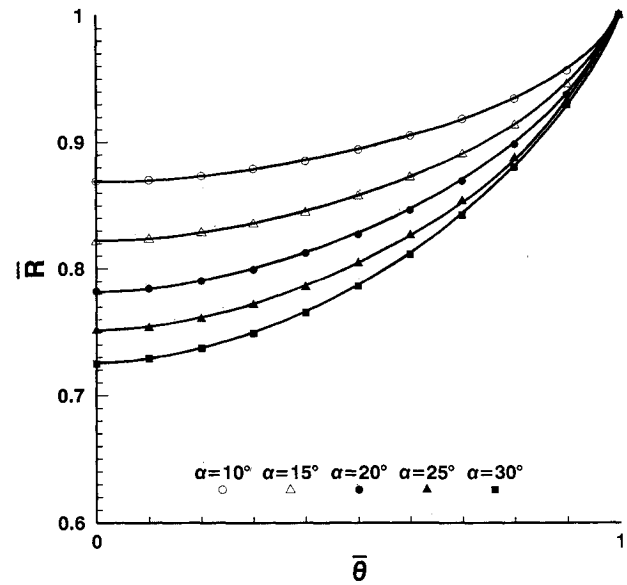

Fig. 3 Normalized meniscus profiles as functions of the wedge half-angle.

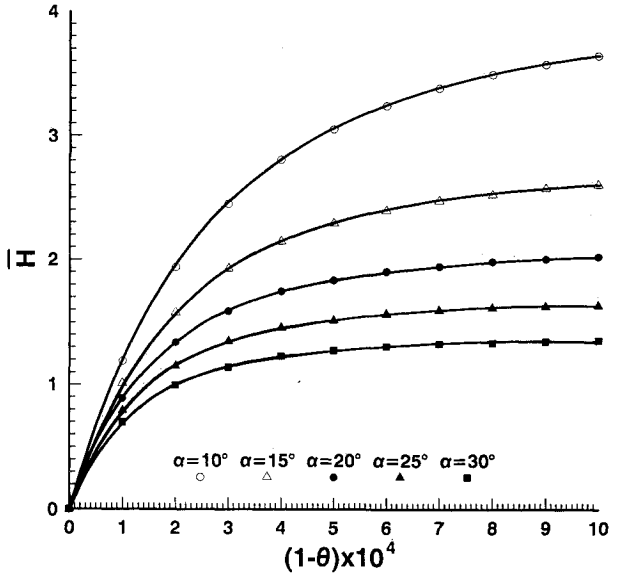

Fig. 4 Mean curvature in the transition region between the interline and the intrinsic meniscus. Note that $\bar{H} = r_0 H$ where $r_0 = 10^{-4}$ m.

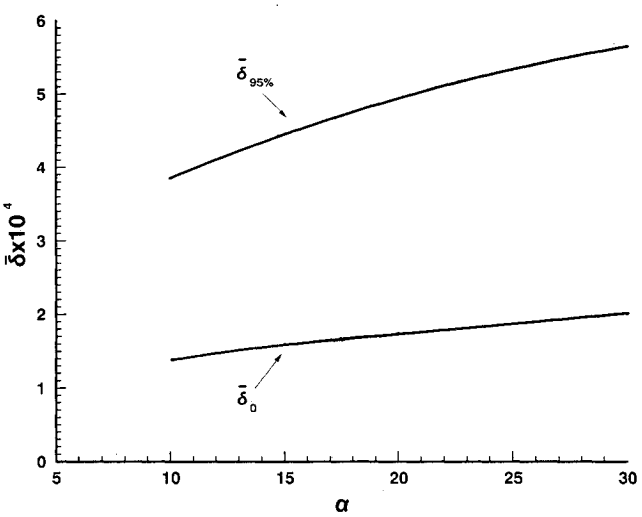

Fig. 5 Layer thickness at the edge of the intrinsic meniscus and adsorbed layer thickness as functions of the wedge half-angle. Note that $\bar{\delta} = \delta/r_0$, where $r_0 = 10^{-4}$ m and $\delta = 0(10^{-8}$ m).

the intrinsic meniscus profile changed very little axially. The figure shows that the Nusselt number decreases exponentially as the wedge half-angle increases. This occurs because the meniscus heat flux is nearly fixed for a constant heat flux number, while the average temperature difference increases as the wedge half-angle increases. Larger average temperature differences (or lower interfacial temperatures) result because the meniscus arc length (or surface area) increases for larger half-angles. This argument is supported by Fig. 3 which shows the normalized meniscus profiles as a function of the wedge half-angle. Note that the actual azimuthal coordinate is $\theta = \alpha\bar{\theta}$; thus θ for $\alpha = 10$ deg is a factor of three less than that for $\alpha = 30$ deg. The increase in meniscus arc length also provides a larger cross-sectional area which can sustain larger mass flow rates.

Figure 4 illustrates the change in the mean curvature profile in the transition region between the interline and intrinsic meniscus for the various wedge half-angles. The mean curvature is equal to zero at the interline as mandated by the wall boundary condition, and increases asymptotically to a constant equal to one-half the capillary pressure. Note that the zero abscissa in the figure represents the edge of the interline, or stationary adsorbed layer, whose thickness is also dependent on the capillary pressure in the intrinsic meniscus. At first glance it appears as though the transition region between the interline and the intrinsic meniscus moves away from the wall as the wedge half-angle decreases. However, the apparent trend shown by the figure is actually disguised by the normalized abscissa.

This point is clarified in Fig. 5, which shows the film thickness at the edge of the intrinsic meniscus where the mean curvature reaches 95% of its asymptotic value ($\bar{\delta}_{95\%}$). The film thickness is calculated from $\bar{\delta} = \bar{R}[\alpha(1 - \bar{\theta}) + \bar{\varepsilon}_0]$ which includes the adsorbed layer thickness, $\bar{\delta}_0 = \bar{R}_0\bar{\varepsilon}_0$. $\bar{\delta}_0$ is also shown in Fig. 5 for reference purposes. The figure indicates that the transition region moves outward away from the wall as the wedge half-angle increases. This occurs for two reasons. The first reason is because the small relative slope of a large half-angle causes the thin film to sustain itself longer. This behavior can be explained more clearly by considering a wedge half-angle of nearly 90 deg, which closely approximates a flat plate. In this case, the meniscus simply becomes a thin film of almost zero mean curvature, and the disjoining pressure plays an important role over the entire film domain. Although this example represents an extreme case, it demonstrates how the thin film is sustained by increasing the wedge half-angle. The second reason why the

transition region moves away from the wall is because the adsorbed layer above the interline increases as the wedge half-angle increases. This is explicitly shown by the lower curve in Fig. 5. Dividing the corresponding points for $\bar{\delta}_{95\%}$ by $\bar{\delta}_0$, and averaging, produces nearly a constant film thickness ratio, namely $\bar{\delta}_{95\%}/\bar{\delta}_0 = 2.80 \pm 0.06$. Therefore, in all cases considered, the disjoining pressure can be neglected for a film thickness greater than three times the adsorbed layer thickness. This bears sharp contrast to the results of Swanson and Herdt[16] for a meniscus in a capillary tube. Their results showed that the mean curvature was asymptotic to a constant beyond a film thickness of approximately 10 times the adsorbed layer thickness. We believe this difference in asymptotic behavior is primarily geometrical in nature. It is also important to note that a retarded form of the disjoining pressure, which is more realistic than the nonretarded form used in this article, will reduce the magnitude of the disjoining pressure even further. This, in effect, will shrink the transition region between the intrinsic meniscus and interline further and expand the domain of the intrinsic meniscus.

Figure 6 compares the actual dimensionless capillary pressure in the intrinsic meniscus, $2\bar{H}/Ca$ [calculated using Eq. (23)], with an approximate value obtained by assuming a semicircular meniscus with a zero adsorbed layer thickness and tangent line at the wall ($1/Ca \tan \alpha$). The approximate form underpredicts the actual capillary pressure by nearly a factor of 2. We believe this discrepancy is due to the presence of the disjoining pressure (van der Waals attraction) near the wall. The van der Waals attraction induces a decrease in mean curvature as the meniscus approaches the wall. Moving away from the wall, the van der Walls attraction forces the meniscus to curve toward the plane of symmetry more abruptly, thereby producing a larger mean curvature (or capillary pressure) in the intrinsic meniscus. Therefore, using a simple semicircular approximation to the mean curvature in V-shaped channels can result in a severe deviation from reality. One remedy may be to use the semicircular approximation with a radius of curvature that matches the disjoining pressure boundary condition at the interline, i.e., Eq. (20). This was done previously in an analytical model of triangular-shaped channels.[6] Using this approximation, their semiempirical model generated a minimum film thickness on the order of 2 μm, which is at least an order of magnitude greater than a film thickness of 0.05 μm (500 Å), where the van der Waals attraction is minimal. This inconsistency may explain the sharp discrepancies between typical nonretarded dispersion constants and those determined semiempirically by Xu and Carey.[6] The reader should note that our intent here is not to discredit the application of matching the mean curvature to a disjoining pressure in the transition region. We believe that the form of the normal stress interfacial condition used for the matching procedure should be based on first principles, i.e., Eq. (8).[9,21]

As stated earlier, no significant change in the intrinsic meniscus profile was observed, regardless of the evaporation rate. This seems somewhat counterintuitive until one looks at the effect of thermocapillary convection and pressure recovery in the liquid phase due to evaporation. The ensuing discussion is based on an examination of the global characteristics of the numerical data; figures depicting these characteristics will immediately follow the discussion.

The piezometric pressure is composed of two terms: 1) the dynamic pressure and 2) the gravitational body force. Between the inlet and the first spatial step in the z direction, the flow changed from a nonevaporating state to an evaporating state. This caused significant thermocapillary convection at the first step downstream from the inlet, primarily because the Marangoni number was large ($M = 5.28 \times 10^3$). The thermocapillary effects generated a surface velocity which flowed in the opposite direction (from cold to hot) of the bulk flow. The magnitude of the surface velocity also increased as the evaporation rate increased. In order to satisfy mass continuity, the dynamic axial pressure gradient had to compensate for the thermocapillary effects. Thus, in all cases a large negative axial pressure gradient was observed near the wedge entrance. After a few steps in the axial direction, the surface temperature gradient was sufficiently small so that the thermocapillary effects essentially vanished. It should be noted that the scaled equation set in this study may not adequately characterize phenomena at the inlet, because the flow becomes thermally fully developed over a very short distance: a local aspect ratio (z/r_0) on the order of one. Some of the terms neglected in this study may be important near the inlet where a significant axial temperature gradient exists. Regardless of the inlet condition, we found that a few steps downstream of the inlet, the velocity, temperature, and pressure did not change significantly when the step size in the

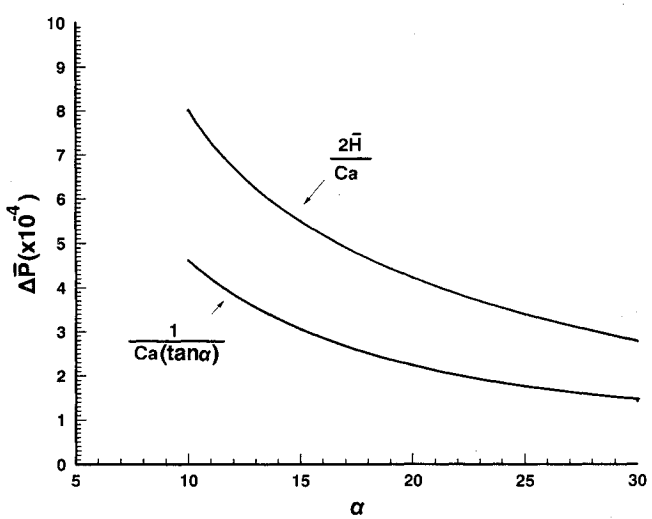

Fig. 6 Exact and approximate forms of the dimensionless capillary pressure difference in the intrinsic meniscus.

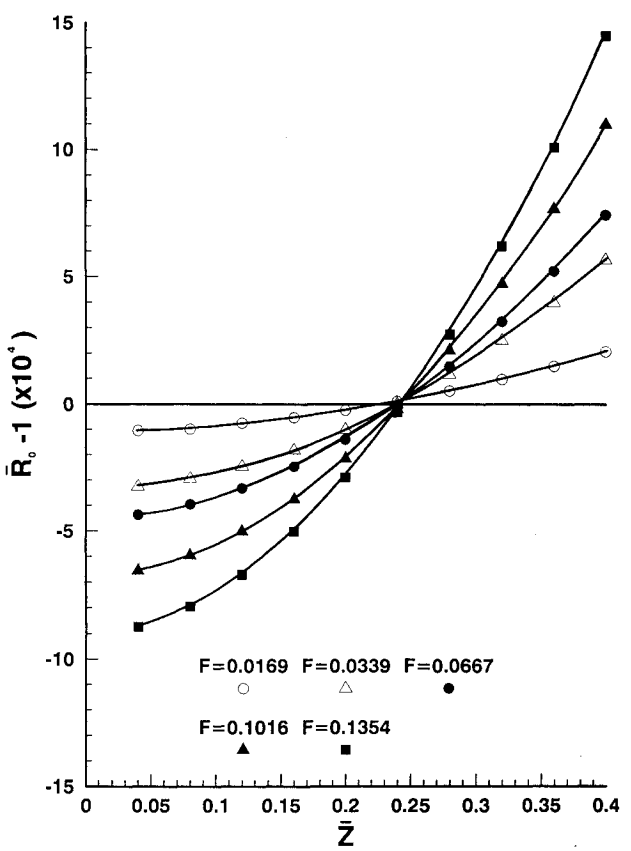

Fig. 7 Interline location as a function of axial position for a wedge half-angle of 30 deg.

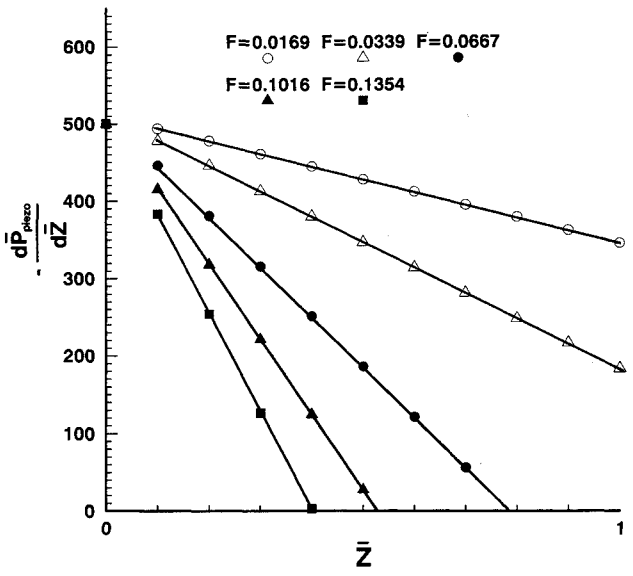

Fig. 8 Axial pressure gradient profiles for a wedge half-angle of 30 deg.

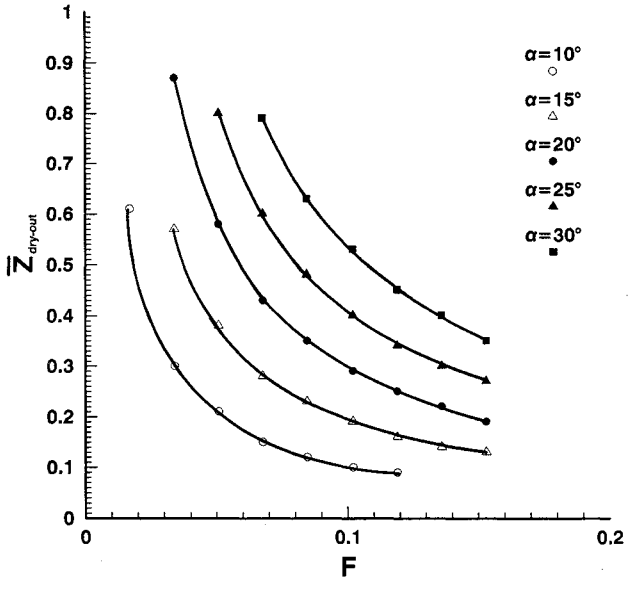

Fig. 9 Estimate of the locus of liquid dry out points as a function of the vapor mass flux number for various wedge half-angles.

axial direction was reduced. Therefore, we are confident that our results are realistic a few steps downstream of the inlet.

The numerical data also showed that downstream from the entrance region, the dynamic pressure gradient eventually changed sign (from negative to positive) due to pressure recovery in the liquid. Beyond this point, the dynamic pressure gradient opposed the gravitational body force and increased steadily in the axial direction until its magnitude was equal to that of the gravitational body force. Since the driving force for flow subsides when the piezometric pressure gradient is equal to zero, we defined this as a liquid dry out condition.

The effects of both thermocapillary convection and pressure recovery can be seen very clearly in Fig. 7, which shows the interline position relative to the inlet position ($\bar{R}_0 = 1$) as a function of axial location for a wedge half-angle of 30 deg. In all cases the interline immediately recedes because of the decrease in liquid pressure due to thermocapillary effects. A decrease in liquid pressure corresponds to an increase in capillary pressure which pushes the meniscus into the wedge. As the mass flux number increases, the interline lowers further into the wedge near the inlet due to an increase in thermocapillary convection. The magnitude of the mass flux number also dictates the amount of pressure recovery in the liquid (or decrease in capillary pressure), which causes the interline to move outward away from the apex. Although the initial interline depression is greater for larger mass flux numbers, the interline rises more rapidly downstream due to the larger pressure recovery. Because the interline continues to rise until the piezometric pressure gradient is equal to zero, we expect an extremely sharp axial decline in the meniscus occurs near the dry out point. Because of the large axial interfacial gradient, accurately capturing specific interface morphological behavior in this region is beyond the scope of the mathematical model developed in this study.

The piezometric pressure gradient profiles associated with a wedge half-angle of 30 deg are plotted in Fig. 8. The large negative piezometric pressure gradients caused by thermocapillary effects near the entrance are not shown in the figure. In all cases, beyond the first axial step, the piezometric pressure gradient decreases linearly downstream from the inlet. The slope of the pressure gradient also increases in magnitude as the mass flux number increases. This occurs because more flow is necessary to feed a larger surface evaporation rate. Note that the lines intersecting the abscissa denote axial dry out points.

The locus of dry out points for various wedge half-angles are plotted in Fig. 9. Recall that these points are only approximations because interfacial phenomena in this region are not completely described by the mathematical model. The figure shows that the dry out location moves closer to the inlet as the surface mass flux increases. As the wedge half-angle increases, the dry out point moves further downstream, because the increase in heat transfer surface area does not sufficiently compensate for the larger mass flow rates. For all wedge half-angles, the dry out location is asymptotic to infinity as the mass flux number goes to zero, which is expected for nonevaporating menisci.

Conclusions

A mathematical model of the evaporating extended meniscus in a V-shaped channel was developed to investigate the effect that wedge half-angle and vapor mass transfer have on meniscus morphology, fluid flow, and heat transfer. The Navier-Stokes and energy equations, as well as the interfacial conditions were scaled using the lubrication approximation. The one-sided formulation was applied to the gas phase under the assumption that the total pressure in the gas phase was constant. The scaled normal stress interfacial condition was also examined in detail to compare the magnitudes of the surface tension forces and van der Waals forces, both near the interline and at the edge of the intrinsic meniscus. The most significant results can be summarized as follows:

1) The average Nusselt number decreased as the wedge half-angle increased.

2) Aside from the dry out region, the shape of the intrinsic meniscus changed very little in the axial direction.

3) The mean curvature changed from zero at the interline to a constant at a distance approximately three times the adsorbed layer thickness from the wall.

4) The capillary pressure calculated from first principles was nearly twice as large as that determined from a semicircular approximation of the mean curvature.

5) Both thermocapillary convection and pressure recovery in the liquid caused the interline to initially move downward toward the wedge apex, and then upward away from the apex until the piezometric pressure was equal to zero.

6) The points where dry out occurred moved toward the inlet as the surface mass flux was increased.

It is apparent that the model developed in this article can be modified for V-shaped channels which are mildly supersaturated and subjected to an axial pressure gradient in the vapor phase (i.e., microheat pipes). The axial pressure gra-

dient in the vapor phase will increase toward the evaporator section and will push the meniscus further into the groove. The resulting increase in the capillary pressure will increase the liquid flow toward the evaporator. Under these conditions, the liquid phase equations also have to be scaled in such a way to retain significant terms in the radial momentum equation. It is well known that for mildly supersaturated liquids, the maximum surface heat flux occurs in the transition region between the interline and the intrinsic meniscus. In this region, the magnitude of the velocity in the radial direction will be on the same order as that in the axial direction. Both viscous losses and variable surface evaporation in the radial direction will significantly affect the radial pressure gradient and the cross-sectional meniscus morphology. We are currently developing a model of the microheat pipe that accounts for these effects.

Essentially, the fluid will be pumped axially from the condenser to the evaporator in the intrinsic meniscus. Evaporation or condensation will occur both on the intrinsic meniscus as well as on the thin film near the interline. Because the maximum heat flux will occur in the interline region, fluid will undoubtedly be pumped into that region. The question is how much. To some degree, the small surface area in the interline region negates the high-heat flux in this region; conversely, the large surface area in the intrinsic meniscus promotes a lower heat flux. Understanding which region dominates is left to a future study.

References

[1]Bressler, R. G., and Wyatt, P. W., "Surface Wetting Through Capillary Grooves," *Journal of Heat Transfer*, Vol. 92, No. 1, 1970, pp. 126–132.

[2]Ayyaswamy, P. S., Catton, I., and Edwards, D. K., "Capillary Flow in Triangular Grooves," *Journal of Applied Mechanics*, Vol. 41, June 1974, pp. 332–336.

[3]Babin, B. R., Peterson, G. P., and Wu, D., "Steady-State Modeling and Testing of a Micro Heat Pipe," *Journal of Heat Transfer*, Vol. 112, No. 3, 1990, pp. 595–601.

[4]Peterson, G. P., Duncan, A. B., Ahmed, A. S., Mallik, A. K., and Weichold, M. H., "Experimental Investigation of Micro Heat Pipes in Silicon Wafers," *Micromechanical Sensors, Actuators, and Systems*, American Society of Mechanical Engineers DSC-Vol. 32, 1991, pp. 341–348.

[5]Edwards, D. K., Balakrishnan, A., and Catton, I., "Power-Law Solutions for Evaporation from a Finned Surface," *Journal of Heat Transfer*, Vol. 96, No. 3, 1974, pp. 423–425.

[6]Xu, X., and Carey, V. P., "Film Evaporation from a Micro-Grooved Surface—An Approximate Heat Transfer Model and Its Comparison with Experimental Data," *Journal of Thermophysics and Heat Transfer*, Vol. 4, No. 4, 1990, pp. 512–520.

[7]Stephan, P. C., and Busse, C. A., "Theoretical Study of an Evaporating Meniscus in a Triangular Groove," *Proceedings of the 7th International Heat Pipe Conference*, Minsk, Russia, May 21–25, 1990.

[8]Burelbach, J. P., Bankoff, S. G., and Davis, S. H., "Nonlinear Stability of Evaporating/Condensing Liquid Films," *Journal of Fluid Mechanics*, Vol. 195, No. 2, 1988, pp. 463–494.

[9]Slattery, J. C., *Interfacial Transport Phenomena*, Springer-Verlag, New York, 1990.

[10]Ivanov, I. B., and Kralchevsky, P. A., "Mechanics and Thermodynamics of Curved Thin Films," *Thin Liquid Films*, edited by I. B. Ivanov, New York, 1988, pp. 99–130.

[11]Adamson, A. W., *Physical Chemistry of Surfaces*, 4th ed., Wiley, New York, 1982.

[12]Van Kampen, N. G., Nijboer, B. R. A., and Schram, K., "On the Macroscopic Theory of van der Waals Forces," *Physics Letters*, Vol. 26A, No. 7, 1968, pp. 307, 308.

[13]Dzyaloshinskii, I. E., Lifshitz, E. M., and Pitaevskii, L. P., "Van der Walls Forces in Liquid Films," *Soviet Physics—JETP* (translation of Izvestiya Vysshikh Uchebnykh Zavedenii, Fizika), Vol. 10, No. 1, 1960, pp. 161–170.

[14]Israelachvili, J. C., *Intermolecular and Surface Forces*, Academic Press, New York, 1985.

[15]Renk, F. J., and Wayner, P. C., Jr., "An Evaporating Ethanol Meniscus Part II: Analytical Studies," *Journal of Heat Transfer*, Vol. 101, No. 1, 1979, pp. 59–62.

[16]Swanson, L. W., and Herdt, G. C., "The Evaporating Meniscus in a Capillary Tube," *Journal of Heat Transfer*, Vol. 114, No. 2, pp. 434–441.

[17]Wayner, P. C., Jr., Kao, Y. K., and LaCroix, L. V., "The Interline Heat-Transfer Coefficient of an Evaporating Wetting Film," *International Journal of Heat and Mass Transfer*, Vol. 19, No. 5, 1976, pp. 487–492.

[18]Wayner, P. C., Jr., "A Constant Heat Flux Model of the Evaporating Interline Region," *International Journal of Heat and Mass Transfer*, Vol. 21, No. 3, 1978, pp. 362–364.

[19]Wayner, P. C., Jr., "Effect of Thin Film Heat Transfer on Meniscus Profile and Capillary Pressure," *AIAA Journal*, Vol. 17, No. 7, 1978, pp. 772–776.

[20]Swanson, L. W., and Peterson, G. P., "The Evaporation Extended Meniscus in a V-Shaped Channel," *Heat Transfer on the Microscale*, American Society of Mechanical Engineers, HTD-Vol. 200, 1992, pp. 9–21.

[21]Patankar, S., *Numerical Heat Transfer and Fluid Flow*, Hemisphere, New York, 1980.

[22]Renk, F. J., Wayner, P. C., Jr., and Homsy, G. M., "On the Transition Between a Wetting Film and a Capillary Meniscus," *Journal of Colloid Science*, Vol. 67, No. 3, 1978, pp. 408–414.

[23]Hornbeck, R. W., *Numerical Methods*, Quantum Publishers, New York, 1975.